FOREWORD

This work was conducted by the National Carbon Company, a Division of Union Carbide Corporation, under USAF Contract AF 33(616)-6915. This contract was initiated under Project No. 7350 "Refractory Inorganic Non-Metallic Materials," Task No. 735002 "Refractory Inorganic Non-Metallic Materials: Graphitic"; Project No. 7381 "Materials Application," Task No. 738102 "Materials Process"; and Project No. 7-817 "Process Development for Graphite Materials." The work was administrated under the direction of the AF Materials Laboratory, Aeronautical Systems Division, with Captain R. H. Wilson, L. J. Conlon, and W. P. Conrardy acting as Project Engineers.

Work under this contract has been in progress since May 1, 1960. The study covered in this report was conducted at the Research Laboratory of the National Carbon Company, located at Parma 30, Ohio, under the direction of J. C. Bowman, Director of Research, and W. P. Eatherly, Assistant Director of Research.

The author would like to thank George B. Spence for his helpful advice and R. Moyer who programmed the numerical calculations on the RPC-4000 digital computer.

Prior reports issued under USAF Contract AF 33(616)-6915 have included:

WADD Technical Notes 61-18 and 61-18, Part II, progress reports covering work from the start of the contract on May 1, 1960, to October 15, 1961, and the following volumes of WADD Technical Report 61-72 covering various subject phases of the work:

Volume I	Observation of Electron Microscopy of Dislocations in Graphite, by R. Sprague.
Volume II	Application of Anisotropic Elastic Continuum Theory to Dislocations in Graphite, by G. B. Spence.
Volume III	Decoration of Dislocations and Low Angle Grain Boundaries in Graphite Single Crystals, by R. Bacon and R. Sprague.
Volume IV	Adaptation of Radiographic Principles to the Quality Control of Graphite, by R. W. Wallouch.
Volume V	Analysis of Creep and Recovery Curves for ATJ Graphite, by E. J. Seldin and R. N. Draper.
Volume VI	Creep of Carbons and Graphites in Flexure at High Temperatures, by E. J. Seldin.

Volume VII	High Density Recrystallized Graphite by Hot Forming, by E. A. Neel, A. A. Kellar, and K. J. Zeitsch.
Volume VIII	Electron Spin Resonance in Polycrystalline Graphite, by L. S. Singer and G. Wagoner.
Volume IX	Fabrication and Properties of Carbonized Cloth Composites, by W. C. Beasley and E. L. Piper.
Volume X	Thermal Reactivity of Aromatic Hydrocarbons, by I. C. Lewis and T. Edstrom.
Volume XI	Characterization of Binders Used in the Fabrication of Graphite Bodies, by E. de Ruiter, A. Halleux, V. Sandor, H. Tschamler.
Volume XII	Development of an Improved Large Diameter Fine Grain Graphite for Aerospace Applications, by C. W. Waters and E. L. Piper.
Volume XIII	Development of a Fine-Grain Isotropic Graphite for Structural and Substrate Applications, by R. A. Howard and E. L. Piper.
Volume XIV	Study of High Temperature Tensile Properties of ZTA Grade Graphite, by R. M. Hale and W. M. Fassell, Jr.
Volume XV	Alumina-Condensed Furfuryl Alcohol Resins, by C. W. Boquist, E. R. Nielsen, H. J. O'Neil, and R. E. Putcher - Armour Research Foundation.
Volume XVI	An Electron Spin Resonance Study of Thermal Reactions of Crganic Compounds, by L. S. Singer and I. C. Lewis.
Volume XVII	Radiography of Carbon and Graphite, by T. C. Furnas, Jr., and M. R. Rosumny.
Volume XVIII	High Temperature Tensile Creep of Graphite, by E. J. Seldin.

ABSTRACT

The equations of thermal stresses and displacements in anisotropic hollow cylinders subjected to various arbitrary temperature boundary conditions have been derived. The hollow cylinder is assumed to be made of transversely isotropic material. Several numerical examples are treated and the effects of the degree of anisotropy on the magnitudes of the critical stress and maximum permissible gas temperature for various sizes of grade ATJ and grade ZTA graphite hollow cylinders are examined. The errors which could result from the assumption of isotropic material are calculated.

This report has been reviewed and is approved.

W. G. RAMKE
Chief, Ceramics and Graphite Branch
Metals and Ceramics Division
AF Materials Laboratory

TABLE OF CONTENTS

LIST OF FIGURES

LIST OF FIGURES (Contd.)

LIST OF TABLES

LIST OF SYMBOLS

T	temperature
T_1, T_R	temperature at r = 1 and r = R
l	relative inside radius
R	relative outside radius, b/a
r	relative radius, $1 \leq r \leq R$
k	thermal conductivity
h	coefficient of heat transfer
κ_r	thermal diffusivity
T_g	gas temperature
r, θ, z	as subscripts designate radial, tangential, and axial directions
ρ	density
c	specific heat
t	time
a	inside radius
b	outside radius
F	heat flux per unit area
β	Biot's modulus, ah/k_r
τ	Fourier's modulus, $\kappa_r t/a^2$
σ	stress
$\sigma_{0,1}$	characteristic stress for Case I, defined by eq. (29e)
$\sigma_{0,2}$	characteristic stress for Case II, defined by eq. (30e)
$\sigma_{0,3}$	characteristic stress for Case III, defined by eq. (31e)
$\bar{\sigma}$	fracture stress
σ^*	maximum relative stress
$\sigma_{r\theta}$, σ_{rz}, $\sigma_{\theta z}$	shearing stresses
ε	engineering strain
s	elastic compliance constants
α_z, α_r	coefficients of linear thermal expansion in axial and radial directions
E_z, E_r	Young's moduli in axial and radial directions
u	relative radial displacement
C_1, C_2	constants of integration
P_1, P_R	internal and external pressures
μ_{zr}	Poisson's ratio = $\frac{\text{contraction in r direction}}{\text{extension in z direction}}$
$\mu_{r\theta}$	Poisson's ratio = $\frac{\text{contraction in } \theta \text{ direction}}{\text{extension in r direction}}$
A	material constant, defined by eq. (11)
B	material constant, defined by eq. (11)

LIST OF SYMBOLS (Contd.)

ξ	material constant, defined by eq. (11)
F_z	normal force across the cross section
J_0	zero-order Bessel function of the first kind
J_1	the first-order Bessel function of the first kind
Y_0	zero-order Bessel function of the second kind
Y_1	the first-order Bessel function of the second kind
a_n	real roots of the transcendental equations of Bessel functions or arguments of Bessel functions
F, U	functions of Bessel functions defined in Table 1

1. INTRODUCTION

In recent years, the unique properties of graphite at elevated temperatures have made it very attractive for high temperature applications in the fields of rockets and missiles. Some of the unique properties of graphite include strength and Young's modulus which increase with increasing temperature, high strength-weight ratio, high thermal shock resistance, and good machinability. On the other hand, graphite is brittle and anisotropic. The degree of anisotropy of graphite is large enough that often it cannot be neglected in the calculations of thermal stresses in the graphite components.

The calculations of thermal stresses generated in rocket nozzles during motor firing is one of the important engineering problems in the missile and rocket industries. The sophisticated and rigorous solutions to this problem are extremely difficult.

The problem can be simplified considerably when the shapes of the nozzles are approximated by hollow cylinders. Almost all work which deals with this problem has been restricted to isotropic materials. Assuming the thermal and physical properties are independent of temperature, Jaeger[1] obtained the expressions for tangential and radial stresses in an isotropic hollow cylinder which is initially at zero temperature and is subjected to radial heat flow according to Newton's Law of Cooling at both surfaces. By suitable choice of the constants in his expressions, the cases of constant temperature, constant flux, convection, or no heat flow at the surfaces can be obtained. Bradshaw[2] plotted the steady-state or maximum tensile stress at the outside surface of an isotropic hollow cylinder against the ratios of inner radius to outer radius for various values of Biot's modulus. Thermal stresses in an isotropic hollow cylinder which has temperature dependent properties have been investigated by Hilton,[3] Chang and Chu,[4] Trostel,[5,6] and Stanišić and McKinley.[7] These investigations considered only the steady-state condition.

Literature on thermal stresses in anisotropic hollow cylinders is quite scarce. Thompson[8] investigated the thermal stress in anisotropic hollow cylinders, but his work is very incomplete. Batchelor et al[9] obtained the expressions for stress components in pyrolytic graphite hollow cylinders under a uniform temperature.

In this investigation the mathematical expressions for stress components and displacements in anisotropic hollow cylinders subjected to various arbitrary temperature boundary conditions are derived. Several numerical examples are treated and the effects of the degree of anisotropy on the stress distributions are examined. Finally, the magnitudes of the critical stress and maximum permissible gas temperature for various sizes of hollow cylinders and temperature boundary conditions are determined.

Manuscript released by the author June 1963 for publication as an ASD Technical Documentary Report.

It is not the purpose of this work to conduct the actual design of the hardware of the rocket nozzles and selection of the proper materials. The results of this investigation, however, can be helpful to engineers who wish to take the anisotropy of the material into account in the design of graphite rocket nozzles.

The present thermal stress analysis is based on linear, uncoupled, quasi-static thermoelasticity. Therefore, the analysis is composed of two distinct problems: heat conduction neglecting the mechanical coupling effect; and elasticity disregarding the inertia effect. The solution of the temperature problem is given in Section 2 and the solution of the elasticity problem is derived in Section 3.

2. TEMPERATURE DISTRIBUTIONS

2.1 Geometry of a Hollow Cylinder

An infinite hollow cylinder having an inside radius of a and an outside radius of b is considered. It is more convenient in the analysis to use the relative radius instead of the actual radius in the cylinder. The relative radius r is defined as the ratio of the actual radius to the inside radius of the cylinder. By this definition the relative inside radius and the relative outside radius of the hollow cylinder become, respectively, 1 and b/a = R. Any relative radius in the hollow cylinder, therefore, is bounded by $1 \leq r \leq R$.

2.2 Boundary Conditions

The actual heat transfer mechanism from the burning propellents to the rocket nozzle is quite complicated and, indeed, little known. However, it will be helpful to assume some idealized thermal boundary conditions and investigate the temperature and stress distributions under these conditions. In this study it is assumed that three different temperature boundary conditions are imposed on a hollow cylinder initially at zero temperature throughout.

Case I: Temperatures at inside and outside surfaces are suddenly increased to finite values:

$$\left.\begin{array}{ll} T = T_1 & \text{at } r = 1 \\ T = T_R & \text{at } r = R \end{array}\right\} \; t > 0.$$

Case II: Constant heat flux is applied to the inside surface and the temperature at the outside surface is suddenly increased to a finite value:

$$\left.\begin{array}{ll} \dfrac{dT}{dr} = -\dfrac{Fa}{k_r} & \text{at } r = 1 \\ T = T_R & \text{at } r = R \end{array}\right\} \; t > 0.$$

Case III: Heat is convected through the inside surface according to Newton's Law of Cooling and the temperature at the outside surface is suddenly increased to a finite value:

$$\left.\begin{array}{ll} k_r \dfrac{dT}{dr} = ah(T - T_g) & \text{at } r = 1 \\ T = T_R & \text{at } r = R \end{array}\right\} \; t > 0.$$

It should be noted that Case I is a special case of Case III. If Biot's modulus $\beta = ah/k_r$ becomes very large, Case III reduces to Case I. Case I

is actually physically impossible and therefore will never occur in practice. Case I is considered in this study because it is the most severe condition theoretically possible under which a rocket nozzle could be fired, and therefore it serves as a limiting case of the firing conditions. In Case II the heat flux per unit area at the inside surface of the cylinder is kept constant at the value F. In Case III, the heat flux across the inside surface of the cylinder is variable and proportional to the temperature drop between the gas temperature T_g and the inside wall temperature T, where the proportionality factor is the heat transfer coefficient h.

The heat transferred during motor firing may be primarily by the process of thermal radiation. The analytical solution of the heat conduction problem with thermal radiation boundary conditions, being nonlinear, is quite difficult. If the bore temperature of the cylinder is small compared to the gas temperature, the thermal radiation case can be approximated by Case II without serious error in the temperature solution. Furthermore, if the bore temperature of the cylinder and the gas temperature do not change appreciably during firing, the thermal radiation boundary condition approaches the convection boundary condition of Case III.

2.3 Solution of the Temperature Problems

The general partial differential equation of heat conduction in cylindrical coordinates is[10]

$$\frac{k_r}{r}\frac{\partial}{\partial r}\left(r\frac{\partial T}{\partial r}\right)+\frac{k_\theta}{r}\frac{\partial^2 T}{\partial \theta^2}+k_z\frac{\partial^2 T}{\partial z^2}=\rho c\frac{\partial T}{\partial t}, \qquad (1)$$

where k_r, k_θ, and k_z are the coefficients of thermal conductivity in radial, tangential, and axial directions; ρ is mass density, and c is specific heat. If it is assumed that heat flows only radially, then equation (1) reduces to

$$\frac{1}{r}\frac{\partial}{\partial r}\left(r\frac{\partial T}{\partial t}\right)=\frac{1}{\kappa_r}\frac{\partial T}{\partial t} \qquad (2)$$

where κ_r is the thermal diffusivity of the material in the radial direction.

The exact solutions of equation (2) which satisfy the above temperature boundary conditions can be found in several articles. The generalized solution given by Jaeger[1] is especially useful. By suitable choice of the constants in the generalized solution, the solutions for these particular cases can be readily obtained and are given in Table 1. The transient solutions are in the form of infinite series of functions of Bessel functions. The arguments of these functions are obtained by solving transcendental equations involving Bessel functions for their roots. Each root is associated with one term of the infinite series. The coefficients of the functions in the infinite series are determined from the initial boundary conditions and the orthogonal relationship between the functions. The first ten terms of the infinite series of functions of Bessel functions have been determined and used in the

Table 1. Temperature Solutions

Case I.

$$\frac{T}{T_1} = \frac{\ell n \frac{R}{r} + \left(\frac{T_R}{T_1}\right) \ell n\, r}{\ell n\, R} - \sum_{n=1}^{\infty} F_1(a_n) U_1(r a_n)\, e^{-a_n^2 \tau} , \qquad (3)$$

where

$$F_1(a_n) = \frac{\pi J_0(Ra_n)\left[J_0(Ra_n) - \left(T_R/T_1\right) J_0(a_n)\right]}{J_0^2(Ra_n) - J_0^2(a_n)}$$

$$U_1(r a_n) = J_0(r a_n) Y_0(a_n) - Y_0(r a_n) J_0(a_n)$$

a_n are the real roots of $U_1(Ra) = 0$

$\tau = K_r t / a^2$.

Case II.

$$\frac{T k_r}{F a} = \ell n \frac{R}{r} + \frac{k_r T_R}{F a} - \sum_{n=1}^{\infty} F_2(a_n) U_2(r a_n) e^{-a_n^2 \tau} , \qquad (4)$$

where

$$F_2(a_n) = \frac{\pi J_0(Ra_n)\left[J_0(Ra_n) - \frac{k_r T_R}{F a}\, a_n J_1(a_n)\right]}{a_n^2\left[J_0^2(Ra_n) - J_1^2(a_n)\right]}$$

$$U_2(r a_n) = a_n\left[J_0(r a_n) Y_1(a_n) - Y_0(r a_n) J_1(a_n)\right]$$

a_n are the real roots of $U_2(Ra) = 0$.

Case III.

$$\frac{T}{T_g} = \frac{\beta \ell n \frac{R}{r} + \left(T_R/T_g\right)(1 + \beta \ell n r)}{1 + \beta \ell n R} - \sum_{n=1}^{\infty} F_3(a_n) U_3(r a_n) e^{-a_n^2 \tau} , \qquad (5)$$

where

$$F_3(a_n) = \frac{-\pi J_0(Ra_n)\left\{ - J_0(Ra_n) + \left(T_R/T_g\right)\left[\frac{a_n}{\beta} J_1(a_n) + J_0(a_n)\right]\right\}}{\left[1 + \left(\frac{a_n}{\beta}\right)^2\right] J_0^2(Ra_n) - \left[\frac{a_n}{\beta} J_1(a_n) + J_0(a_n)\right]^2}$$

$$U_3(r a_n) = \frac{1}{\beta} U_2(r a_n) + U_1(r a_n)$$

a_n are the real roots of $U_3(Ra) = 0$

$\beta = ah/k_r$

numerical temperature and stress calculations. The numerical computations in this work were done on an RPC-4000 digital computer.

2.4 Numerical Calculations of the Temperature Distributions

Temperature distributions in a hollow cylinder with a wall ratio of 2.0 are calculated for various values of Fourier's modulus $\tau = K_r t / a^2$ and are shown in Figures 1 and 2. In all cases the temperature at the outside surface is taken to be zero, which is the initial temperature throughout the cylinder.

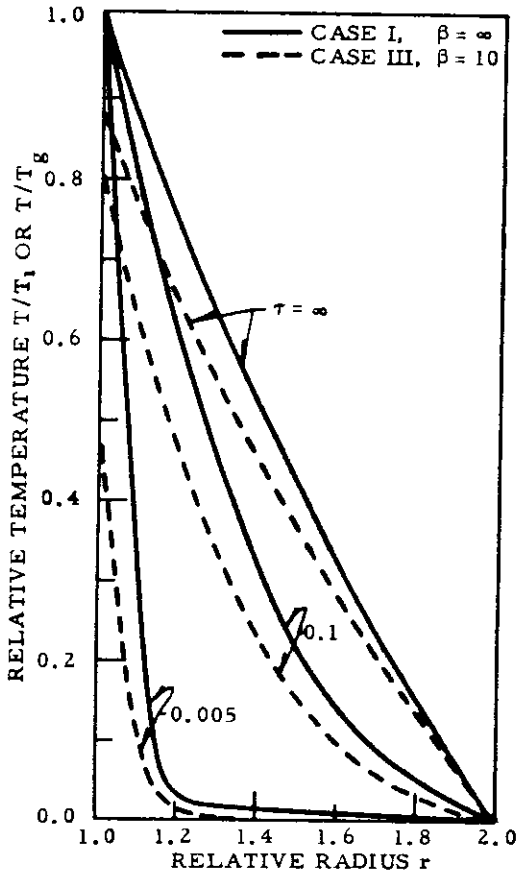

N-3538

Figure 1. Temperature Distribution in Hollow Cylinder with a Wall Ratio of 2.0. Cases I and III.

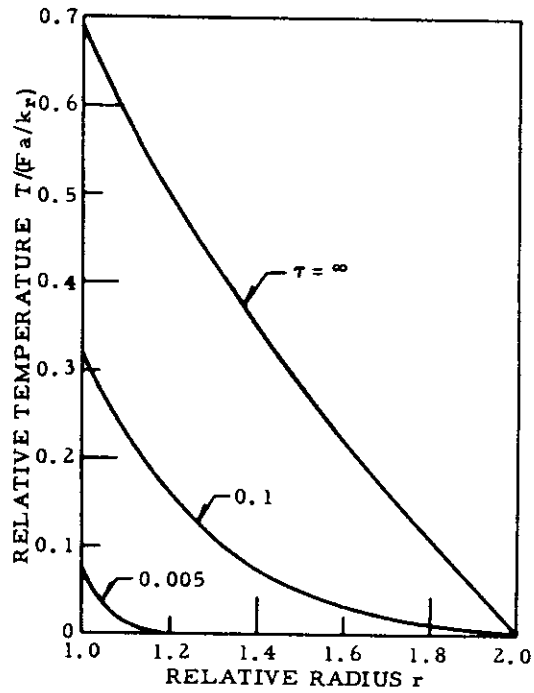

N-4294

Figure 2. Temperature Distribution in a Hollow Cylinder with a Wall Ratio of 2.0. Case II.

Cases I and III are combined in Figure 1 to show the effect of Biot's modulus on the temperature distribution. In Case I the bore temperature becomes the same as the gas temperature. In Case III a Biot's modulus of 10 is assumed. Case II is given in Figure 2. In all cases the maximum temperature occurs at the bore when the steady-state condition is reached in the cylinder. The variation of the maximum temperature for various wall ratios and Biot's moduli is shown in Figure 3.

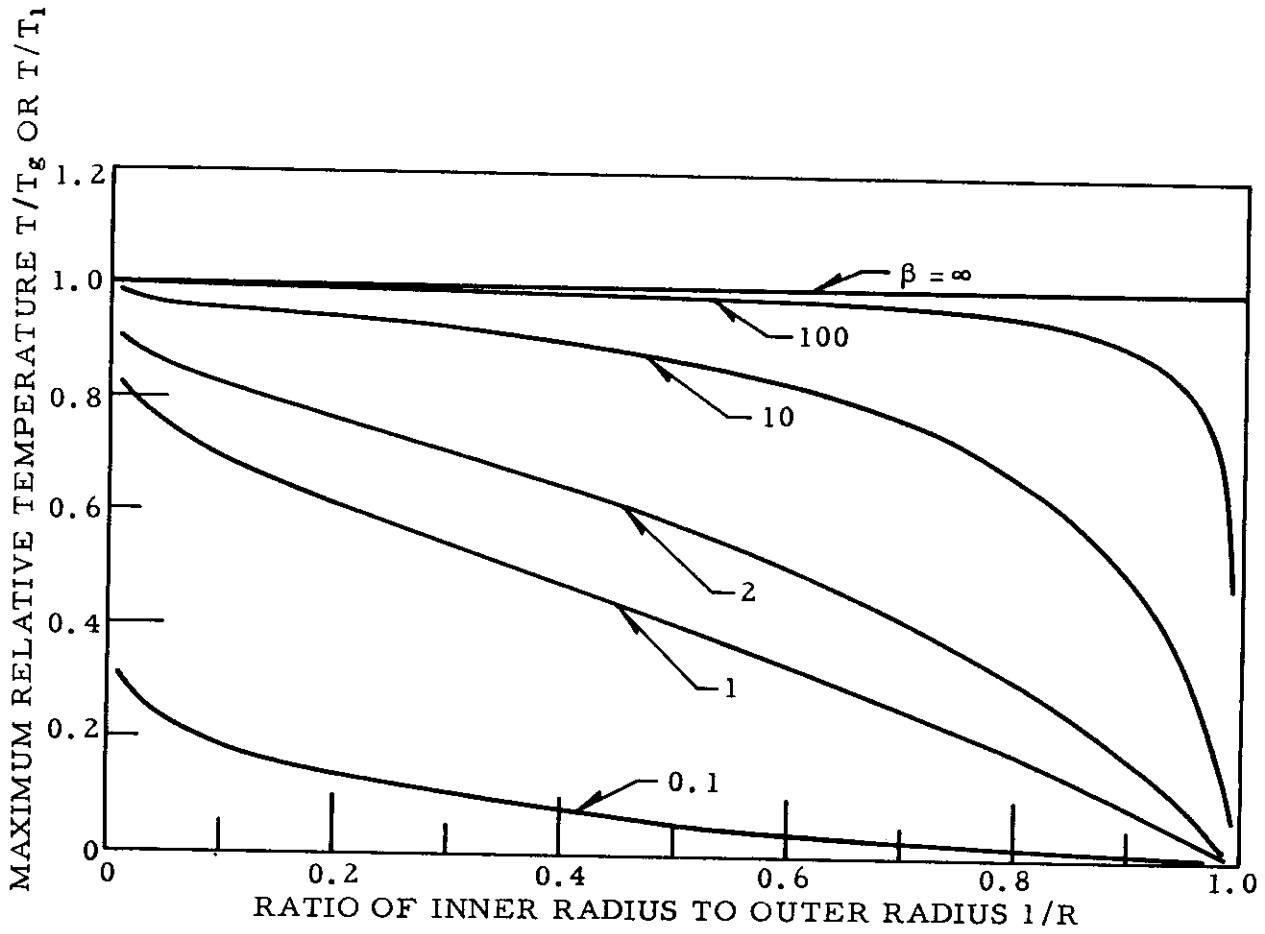

Figure 3. Maximum Temperature at Bore for Various Wall Ratios

3. STRESS DISTRIBUTIONS

3.1 Assumptions

The calculation of thermal stresses in the exact configuration of the nozzle is a complex problem. However, the problem can be simplified greatly, if the shape of the nozzle is approximated by a hollow cylinder. Further simplifying assumptions will be used in the analysis of thermal stresses in the anisotropic hollow cylinder:

(1) Physical and thermal material constants are independent of temperature.

(2) The stress-strain relation of the material obeys Hooke's Law.

(3) The material is assumed to be transversely isotropic. If the properties of the material in the plane perpendicular to the z axis are isotropic and are different from those in the direction of the z axis, the material is called transversely isotropic.

(4) The principal axes of anisotropy coincide with the principal axes of the cylinder.

(5) The condition of plane strain is assumed.

Several points should be noted. First, the physical and thermal properties of the materials are dependent on temperature to various degrees and in various ways. In order to include the variation of the material constants in the thermal stress calculations, the values of the material constants as a function of temperature must be known. In fact these experimental data are not yet completely available for graphite materials. Therefore, as the first phase of the thermal stress calculations of an anisotropic hollow cylinder, the analysis based on the assumption of temperature independent material constants will be made. Second, it can be assumed with sufficient accuracy that most molded graphites are transversely isotropic and that the grain of molded graphites is perpendicular to the direction of the molding pressure. Third, the condition of plane strain is a good approximation for a hollow cylinder which is sufficiently long with respect to its cross-sectional dimensions. Under the condition of plane strain, the stress and strain components become independent of the axial distance z along the length of the cylinder.

3.2 Stress-Strain Relationship

According to the generalized Hooke's law, the stress-strain relation at any point in an elastic solid is given by[11]

$$\left.\begin{aligned}
\varepsilon_1 &= s_{11}\sigma_1 + s_{12}\sigma_2 + s_{13}\sigma_3 + s_{14}\sigma_4 + s_{15}\sigma_5 + s_{16}\sigma_6 \\
\varepsilon_2 &= s_{21}\sigma_1 + s_{22}\sigma_2 + s_{23}\sigma_3 + s_{24}\sigma_4 + s_{25}\sigma_5 + s_{26}\sigma_6 \\
\varepsilon_3 &= s_{31}\sigma_1 + s_{32}\sigma_2 + s_{33}\sigma_3 + s_{34}\sigma_4 + s_{35}\sigma_5 + s_{36}\sigma_6 \\
\varepsilon_4 &= s_{41}\sigma_1 + s_{42}\sigma_2 + s_{43}\sigma_3 + s_{44}\sigma_4 + s_{45}\sigma_5 + s_{46}\sigma_6 \\
\varepsilon_5 &= s_{51}\sigma_1 + s_{52}\sigma_2 + s_{53}\sigma_3 + s_{54}\sigma_4 + s_{55}\sigma_5 + s_{56}\sigma_6 \\
\varepsilon_6 &= s_{61}\sigma_1 + s_{62}\sigma_2 + s_{63}\sigma_3 + s_{64}\sigma_4 + s_{65}\sigma_5 + s_{66}\sigma_6
\end{aligned}\right\} \qquad (6)$$

where as ε_i is the engineering strain component, σ_j is the stress component, and s_{ij} is the elastic compliance constant.

Six components of stress are related to six components of strain by means of 36 elastic compliance constants in these equations. Because of the symmetric property, $s_{ij} = s_{ji}$, of these elastic compliance constants and the symmetry of transversely isotropic material, the elastic compliance constants are reduced to five, namely, s_{11}, s_{12}, s_{13}, s_{33}, and s_{44}. The stress distribution in a hollow cylinder under radial heat flow or internal and external pressures is axially symmetric. On account of this symmetry, the shear stresses σ_4, σ_5, and σ_6 vanish and hence s_{44} does not occur in the analysis. If the temperature of the elastic solid is raised, the total strains at any point are the sum of the strains due to linear thermal expansion of the solid and the strains given by Hooke's law. Therefore, the stress-strain relations for molded graphites at elevated temperatures become

$$\left.\begin{aligned}
\varepsilon_1 &= s_{11}\sigma_1 + s_{12}\sigma_2 + s_{13}\sigma_3 + \alpha_1 T \\
\varepsilon_2 &= s_{12}\sigma_1 + s_{11}\sigma_2 + s_{13}\sigma_3 + \alpha_1 T \\
\varepsilon_3 &= s_{13}\sigma_1 + s_{13}\sigma_2 + s_{33}\sigma_3 + \alpha_3 T.
\end{aligned}\right\} \qquad (7)$$

Since the problem deals with the stresses in a hollow cylinder, it will be more convenient to write the stress-strain relations in the cylindrical coordinates (r, θ, and z). By the assumptions (3) and (4), the r-θ plane in the cylinder represents the basal plane (1-2 plane) of graphites and the z axis of the cylinder is parallel with the c or 3 axis of graphites. Replacing the notations in equation (7) by 1 $\longleftrightarrow$ r, 2 $\longleftrightarrow$ θ, and 3 $\longleftrightarrow$ z, and using the simplifications: 11 $\longleftrightarrow$ r and 33 $\longleftrightarrow$ z, the stress-strain relations in the cylindrical coordinates become

$$\varepsilon_r = s_r\sigma_r + s_{r\theta}\sigma_\theta + s_{zr}\sigma_z + \alpha_r T \qquad (8a)$$

$$\varepsilon_\theta = s_{r\theta}\sigma_r + s_r\sigma_\theta + s_{zr}\sigma_z + \alpha_r T \qquad (8b)$$

$$\varepsilon_z = s_{zr}\sigma_r + s_{zr}\sigma_\theta + s_z\sigma_z + \alpha_z T. \qquad (8c)$$

The elastic compliance constants in equations (8) can be written in terms of the Young's moduli and Poisson's ratios as

$$\left.\begin{aligned} s_r &= \frac{1}{E_r} \\ s_z &= \frac{1}{E_z} \end{aligned}\right\} \qquad \left.\begin{aligned} s_{r\theta} &= -\frac{\mu_{r\theta}}{E_r} \\ s_{zr} &= -\frac{\mu_{zr}}{E_z} \end{aligned}\right\} \tag{9}$$

where E_r and E_z are the Young's moduli in radial and axial directions, $\mu_{r\theta}$ is the ratio of the contraction in the θ direction to the extension in the r direction, and μ_{zr} is the ratio of the contraction in the r direction to the extension in the z direction.

3.3 Tangential and Radial Stresses

Solving equations (8) for σ_θ, σ_r, and σ_z, one gets

$$\sigma_\theta = \frac{1}{B^2 - A^2}\left[-A\varepsilon_r + B\varepsilon_\theta + \frac{s_{zr}}{s_z}(A-B)\varepsilon_z + \xi(A-B)T\right] \tag{10a}$$

$$\sigma_r = \frac{1}{B^2-A^2}\left[B\varepsilon_r - A\varepsilon_\theta + \frac{s_{zr}}{s_z}(A-B)\varepsilon_z + \xi(A-B)T\right] \tag{10b}$$

$$\sigma_z = \frac{1}{s_z}\left[\varepsilon_z - s_{zr}(\sigma_r + \sigma_\theta) - \alpha_z T\right] \tag{10c}$$

where

$$\left.\begin{aligned} A &= \frac{s_{r\theta}\, s_z - s^2_{zr}}{s_z} = -\frac{\mu_{r\theta}}{E_r} - \frac{\mu^2_{zr}}{E_z} \\ B &= \frac{s_r s_z - s^2_{zr}}{s_z} = \frac{1}{E_r} - \frac{\mu^2_{zr}}{E_z} \\ \xi &= \frac{s_z \alpha_r - s_{zr}\alpha_z}{s_z} = \alpha_r + \alpha_z \mu_{zr}\,. \end{aligned}\right\} \tag{11}$$

For the isotropic case the constants above become

$$A = -\frac{\mu(1+\mu)}{E} \qquad B = \frac{1-\mu^2}{E} \qquad \xi = \alpha(1+\mu)\,. \tag{12}$$

The equations of equilibrium in the cylindrical coordinates are[12]

$$\left.\begin{aligned} &\frac{\partial \sigma_r}{\partial r} + \frac{1}{r}\frac{\partial \sigma_{r\theta}}{\partial \theta} + \frac{\partial \sigma_{rz}}{\partial z} + \frac{\sigma_r - \sigma_\theta}{r} + R' = 0 \\ &\frac{\partial \sigma_{r\theta}}{\partial r} + \frac{1}{r}\frac{\partial \sigma_\theta}{\partial \theta} + \frac{\partial \sigma_{\theta z}}{\partial z} + \frac{2}{r}\sigma_{r\theta} + \theta' = 0 \\ &\frac{\partial \sigma_{rz}}{\partial r} + \frac{1}{r}\frac{\partial \sigma_{\theta z}}{\partial \theta} + \frac{\partial \sigma_z}{\partial z} + \frac{1}{r}\sigma_{rz} + Z' = 0 , \end{aligned}\right\} \qquad (13)$$

where R', θ', and Z' are the body-force components in the r, θ, and z directions. Because of the absence of the body forces and the conditions of plane strain and axial symmetry, the first equation of equilibrium becomes

$$\frac{d\sigma_r}{dr} + \frac{\sigma_r - \sigma_\theta}{r} = 0 \qquad (14)$$

and the second and third equations of equilibrium are identically satisfied.

If u is the relative radial displacement (actual radial displacement divided by inner radius) at the relative radius r, then the radial and tangential strain components under axial symmetry and the condition of plane strain[12] can be written in terms of u as

$$\varepsilon_r = \frac{du}{dr} \qquad (15a)$$

$$\varepsilon_\theta = \frac{u}{r} \qquad (15b)$$

The differential equation for the radial displacement u, obtained from equations (10), (14), and (15) is

$$\frac{d^2u}{dr^2} + \frac{1}{r}\frac{du}{dr} - \frac{u}{r^2} = \frac{\xi(B - A)}{B}\frac{dT}{dr} . \qquad (16)$$

The solution of equation (16), obtained by integrating twice, is

$$u = \frac{\xi(B - A)}{Br}\int_1^r Trdr + C_1 r + \frac{C_2}{r} , \qquad (17)$$

where C_1 and C_2 are constants of integration which are to be determined from the stress conditions at the inside and outside surfaces. If the cylinder is subjected to both internal and external pressures, the boundary conditions will be

$$\sigma_r = -P_1 \qquad \text{at } r = 1$$

$$\sigma_r = -P_R \qquad \text{at } r = R. \tag{18}$$

The constants of integration C_1 and C_2 can be determined from equations (15), (17), (10b), and the boundary conditions given by equation (18). Combining equations (10), (15), and (17), and these constants, the following expressions for the tangential and radial stresses are derived:

$$\sigma_\theta = \frac{\xi}{B}\left[\frac{1}{r^2}\int_1^r Trdr + \frac{r^2+1}{(R^2-1)r^2}\int_1^R Trdr - T\right] + \frac{R^2(P_1-P_R)}{(R^2-1)r^2} + \frac{P_1 - R^2P_R}{R^2-1} \tag{19}$$

$$\sigma_r = \frac{\xi}{B}\left[\frac{r^2-1}{(R^2-1)r^2}\int_1^R Trdr - \frac{1}{r^2}\int_1^r Trdr\right] - \frac{R^2(P_1-P_R)}{(R^2-1)r^2} + \frac{P_1 - R^2P_R}{R^2-1}. \tag{20}$$

It should be noted that, similar to the isotropic case, the tangential and radial stresses are independent of the end condition of the cylinder. Equations (19) and (20) can be reduced to the isotropic case when ξ/B is replaced by $\alpha E/1-u$. It should be noted also that the total stresses can be obtained by superimposing the stresses generated by the temperature and the stresses produced by the pressures and that the stresses due to the pressures are independent of material properties.

3.4 Axial Stresses and Radial Displacements

The expression for the axial stress, obtained by substituting equations (19) and (20) into equation (10c), is

$$\sigma_z = \frac{1}{s_z}\left\{-\left(\frac{\xi s_{zr}}{B}\right)\frac{2}{R^2-1}\int_1^R Trdr - \left(\frac{\alpha_z B - \xi s_{zr}}{B}\right)T + \varepsilon_z - 2s_{zr}\left(\frac{P_1 - R^2P_R}{R^2-1}\right)\right\} \tag{21}$$

Equation (21) gives the axial stress for the case of generalized plane strain. The total normal force across the cross section of the cylinder is

$$F_z = 2\pi a^2\int_1^R \sigma_z r dr. \tag{22}$$

The axial stress distribution given by equation (21) is accurate for an infinite cylinder. Equation (21) also is a good approximation for a finite cylinder, according to Saint-Venant's principle, at regions of the cylinder which are at a distance from the ends larger than the outside diameter of the cylinder.

Two cases of plane strain are of particular interest: namely, (a) the axial elongation is prevented by end constraints, that is $\varepsilon_z = 0$, and (b) the ends of the cylinder are free in the sense that the total normal force across the cross-sectional area of the cylinder is zero, that is, $F_z = 0$.

(a) Zero Axial Strain, $\varepsilon_z = 0$

Setting ε_z in equation (21) equal to zero, the axial stress for this case is obtained:

$$\sigma_z = \frac{a_z B - \xi s_{zr}}{s_z B}\left(\frac{2}{R^2-1}\int_1^R Trdr - T\right) - \left(\frac{a_z}{s_z}\right)\frac{2}{R^2-1}\int_1^R Trdr - \frac{2s_{zr}}{s_z}\left(\frac{P_1 - R^2 P_R}{R^2-1}\right). \quad (23)$$

The radial displacement for this case, by setting $\varepsilon_z = 0$ in the expressions for C_1 and C_2 and then substituting C_1 and C_2 into equation (17), becomes

$$u = \frac{\xi(B-A)}{Br}\int_1^r Trdr + \frac{\xi s_z(B-A) + \left[\xi s_z(A+B) + 2s_{zr}a_z B\right] r^2}{B(R^2-1)rs_z}\int_1^R Trdr - \frac{2s_{zr}a_z r}{(R^2-1)s_z}\int_1^R Trdr + (A+B)\left[\frac{(P_1 - R^2P_R)r}{R^2-1}\right] + (s_r - s_{\theta r})\left[\frac{R^2(P_1 - P_R)}{(R^2-1)r}\right] \quad (24)$$

(b) Zero Normal Force, $F_z = 0$

In order to obtain this condition, the external forces must be applied to the ends of the cylinder in such a way that the sum of the normal forces on the cross section of the cylinder is zero, or

$$F_z = a^2\int_1^R \sigma_z 2\pi r dr = 0$$

By equation (21) and the condition $F_z = 0$, the magnitude of the axial strain is found to be

$$\varepsilon_z = \frac{2a_z}{R^2 - 1} \int_1^R Trdr + 2s_{zr} \left(\frac{P_1 - R^2 P_R}{R^2 - 1} \right). \tag{25}$$

Substituting ε_z given by equation (25) into equation (21), the desired expression for the axial stress becomes

$$\sigma_z = \frac{a_z B - \xi s_{zr}}{s_z B} \left(\frac{2}{R^2 - 1} \int_1^R Trdr - T \right) . \tag{26}$$

The axial stress in this case is not affected by the presence of the pressure.

Under the absence of the pressures the sum of the tangential and radial stresses is always equal to the axial stress for the isotropic case; however, this relationship does not hold any longer for the anisotropic case. The sum of σ_r and σ_θ for the anisotropic case is related to σ_z for Case (b) by

$$\sigma_r + \sigma_\theta = \left(\frac{\xi s_z}{a_z B - \xi s_{zr}} \right) \sigma_z = \frac{E_r(\mu_{zr} a_z + a_r)}{\mu_{zr} a_r E_r + a_z E_z} \sigma_z . \tag{27}$$

The value of the factor in equation (27) is less than 1.0 for grade ATJ and grade ZTA graphites and equal to 1.0 for the isotropic case. Therefore, for Case (b) the axial stress is always larger than the sum of the tangential and radial stresses for a graphite cylinder which has the assumed grain orientation. Consequently, the critical stress in such a cylinder will be the axial stress at either the bore or the outside surface.

Combining equations (17), (25), and the expressions for C_1 and C_2, the radial displacement for Case (b) is found to be

$$u = \frac{\xi(B-A)}{Br} \int_1^r Trdr + \frac{\xi s_z (B-A) + [\xi s_z (A+B) + 2 s_{zr} a_z B] r^2}{B(R^2 - 1) r\, s_z} \int_1^R Trdr$$

$$+ (s_r + s_{\theta r}) \frac{(P_1 - R^2 P_R) r}{(R^2 - 1)} + (s_r - s_{\theta r}) \frac{R^2 (P_1 - P_R)}{(R^2 - 1) r} . \tag{28}$$

The final expressions for the stresses and radial displacements can be obtained when the temperature T in equations (19), (20), (23), (24), (26), and

(28) is replaced by the temperature solutions given in the previous section. The tangential, radial, and axial stresses for three cases of temperature boundary conditions are given in Tables 2, 3, and 4. U and F are functions of Bessel functions and are already given in Table 1. U' and F' denote the derivatives of the functions with respect to r. The quantities ξ and B are the material constants given in equation (11). The general solutions for the stresses for the anisotropic material can be obtained by replacing $\alpha E/1-\mu$ in Jaeger's solution[1] with ξ/B. The final forms of the radial displacements are not given, but they can be obtained readily in a similar way.

Table 2. Stress Solutions for Case I

Tangential Stress

$$\frac{\sigma_\theta}{\sigma_{0,1}} = \frac{\frac{T_R}{T_1} - 1}{2\ell nR}\left[\frac{R^2(r^2+1)}{r^2(R^2-1)}\ell nR - 1 - \ell nr\right] + \sum_{n=1}^{\infty}\frac{F_1(a_n)e^{-a_n^2\tau}}{a_n^2}\left[\frac{R(r^2+1)}{r^2(R^2-1)}U_1'(Ra_n) + \frac{U_1'(ra_n)}{r} + a_n^2U_1(ra_n) + \frac{2(R^2+r^2)}{\pi(R^2-1)r^2}\right]$$

$$+\frac{1}{\sigma_{0,1}}\left[\frac{R^2(P_1-P_R)}{(R^2-1)r^2} + \frac{P_1-R^2P_R}{R^2-1}\right] \qquad (29a)$$

Radial Stress

$$\frac{\sigma_r}{\sigma_{0,1}} = \frac{\frac{T_R}{T_1}-1}{2\ell nR}\left[\frac{R^2(r^2-1)}{r^2(R^2-1)}\ell nR - \ell nr\right] - \sum_{n=1}^{\infty}\frac{F_1(a_n)e^{-a_n^2\tau}}{a_n^2}\left[\frac{U_1'(ra_n)}{r} - \frac{R(r^2-1)}{r^2(R^2-1)}U_1'(Ra_n) + \frac{2(R^2-r^2)}{\pi(R^2-1)r^2}\right]$$

$$-\frac{1}{\sigma_{0,1}}\left[\frac{R^2(P_1-P_R)}{(R^2-1)r^2} - \frac{P_1-R^2P_R}{R^2-1}\right] \qquad (29b)$$

Axial Stress

Case (a): $\epsilon_z = 0$

$$\left(\frac{\xi S_z}{a_zB - \xi S_{zr}}\right)\frac{\sigma_z}{\sigma_{0,1}} = \frac{\frac{T_R}{T_1}-1}{\ell nR}\left(\frac{R^2\ell nR}{R^2-1} - \ell nr - \tfrac{1}{2}\right) + \sum_{n=1}^{\infty}\frac{F_1(a_n)e^{-a_n^2\tau}}{a_n^2}\left[\frac{2R}{R^2-1}U_1'(Ra_n) + a_n^2U_1(ra_n) + \frac{4}{\pi(R^2-1)}\right]$$

$$-\left(\frac{a_zB}{a_zB - \xi S_{zr}}\right)\left\{\frac{R^2(\frac{T_R}{T_1})-1}{R^2-1} + \frac{\frac{T_R}{T_1}-1}{2\ell nR} + \sum_{n=1}^{\infty}\frac{F_1(a_n)e^{-a_n^2\tau}}{a_n^2}\left[\frac{2R}{R^2-1}U_1'(Ra_n) + \frac{4}{\pi(R^2-1)}\right]\right\}$$

$$+\frac{2S_{zr}}{S_z\sigma_{0,1}}\left(\frac{\xi S_z}{a_zB - \xi S_{zr}}\right)\left(\frac{P_1-R^2P_R}{R^2-1}\right) \qquad (29c)$$

Case (b): $F_z = 0$

$$\left(\frac{\xi S_z}{a_zB - \xi S_{zr}}\right)\frac{\sigma_z}{\sigma_{0,1}} = \frac{\frac{T_R}{T_1}-1}{\ell nR}\left(\frac{R^2\ell nR}{R^2-1} - \ell nr - \tfrac{1}{2}\right) + \sum_{n=1}^{\infty}\frac{F_1(a_n)e^{-a_n^2\tau}}{a_n^2}\left[\frac{2R}{R^2-1}U_1'(Ra_n) + a_n^2U_1(ra_n) + \frac{4}{\pi(R^2-1)}\right] \qquad (29d)$$

Characteristic Stress

$$\sigma_{0,1} = \frac{\xi T_1}{B} = \frac{E_rE_z(a_z\mu_{zr} + a_r)T_1}{E_z - \mu_{zr}^2E_r} \qquad (29e)$$

Table 3. Stress Solutions for Case II

Tangential Stress

$$\frac{\sigma_\theta}{\sigma_{0,z}} = \frac{1}{2}\left[\ell nr + 1 - \frac{R^2(r^2+1)}{r^2(R^2-1)}\ell nR\right] + \sum_{n=1}^{\infty} \frac{F_z(a_n)e^{-a_n^2\tau}}{a_n^2}\left[\frac{R(r^2+1)}{r^2(R^2-1)}U_2^1(Ra_n) + \frac{1}{r}U_2^1(ra_n) + a_n^2U_2(ra_n)\right] + \frac{1}{\sigma_{0,z}}\left[\frac{R^2(P_1-P_R)}{(R^2-1)r^2} + \frac{P_1 - R^2P_R}{R^2-1}\right] \quad (30a)$$

Radial Stress

$$\frac{\sigma_r}{\sigma_{0,z}} = \frac{1}{2}\left[\ell nr - \frac{R^2(r^2-1)}{r^2(R^2-1)}\ell nR\right] - \sum_{n=1}^{\infty} \frac{F_z(a_n)e^{-a_n^2\tau}}{a_n^2}\left[\frac{1}{r}U_2^1(ra_n) - \frac{R(r^2-1)}{r^2(R^2-1)}U_2^1(Ra_n)\right] - \frac{1}{\sigma_{0,z}}\left[\frac{R^2(P_1-P_R)}{(R^2-1)r^2} - \frac{P_1 - R^2P_R}{R^2-1}\right] \quad (30b)$$

Axial Stress

Case (a): $\epsilon_z = 0$

$$\left(\frac{\xi S_z}{a_z B - \xi S_{zr}}\right)\frac{\sigma_z}{\sigma_{0,z}} = \left(\frac{1}{2} + \ell nr - \frac{R^2\ell nR}{R^2-1}\right) + \sum_{n=1}^{\infty} \frac{F_z(a_n)e^{-a_n^2\tau}}{a_n^2}\left[\frac{2R}{R^2-1}U_2^1(Ra_n) + a_n^2U_2(ra_n)\right] - \left(\frac{a_z B}{a_z B - \xi S_{zr}}\right)\left[\frac{1}{2} - \frac{\ell nR}{R^2-1} + \frac{k_r T_R}{Fa} + \frac{2R}{R^2-1}\sum_{n=1}^{\infty}\frac{F_z(a_n)e^{-a_n^2\tau}}{a_n^2}U_2^1(Ra_n)\right] - \frac{2S_{zr}}{S_z\sigma_{0,z}}\left(\frac{\xi S_z}{a_z B - \xi S_{zr}}\right)\left(\frac{P_1 - R^2P_R}{R^2-1}\right) \quad (30c)$$

Case (b): $F_z = 0$

$$\left(\frac{\xi S_z}{a_z B - \xi S_{zr}}\right)\frac{\sigma_z}{\sigma_{0,z}} = \left(\frac{1}{2} + \ell nr - \frac{R^2\ell nR}{R^2-1}\right) + \sum_{n=1}^{\infty} \frac{F_z(a_n)e^{-a_n^2\tau}}{a^2}\left[\frac{2R}{R^2-1}U_2^1(Ra_n) + a_n^2U_2(ra_n)\right] \quad (30d)$$

Characteristic Stress

$$\sigma_{0,z} = \frac{\xi}{B}\left(\frac{Fa}{k_r}\right) = \frac{E_r E_z(a_z\mu_{zr} + a_r)}{E_z - \mu_{zr}^2 E_r}\left(\frac{Fa}{k_r}\right) \quad (30e)$$

Table 4. Stress Solution for Case III

Tangential Stress

$$\frac{\sigma_\theta}{\sigma_{0,3}} = \frac{\beta\left(\frac{T_R}{T_g} - 1\right)}{2(1+\beta \ell nR)} \left[\frac{R^2(r^2+1)}{r^2(R^2-1)} \ell nR - 1 - \ell nr\right] + \sum_{n=1}^{\infty} \frac{F_3(a_n)e^{-a_n^2\tau}}{a_n^2} \left[a_n^2 U_3(ra_n) + \frac{R(r^2+1)}{r^2(R^2-1)} U_3^1(Ra_n) + \frac{1}{r} U_3^1(ra_n) + \frac{2(R^2+r^2)}{\pi r^2(R^2-1)}\right]$$

$$+ \frac{1}{\sigma_{0,3}}\left[\frac{R^2(P_1 - P_R)}{(R^2-1)r^2} + \frac{P_1 - R^2P_R}{R^2-1}\right] \qquad (31a)$$

Radial Stress

$$\frac{\sigma_r}{\sigma_{0,3}} = \frac{\beta\left(\frac{T_R}{T_g} - 1\right)}{2(1+\beta \ell nR)} \left[\frac{R^2(r^2-1)}{r^2(R^2-1)} \ell nR - \ell nr\right] - \sum_{n=1}^{\infty} \frac{F_3(a_n)e^{-a_n^2\tau}}{a_n^2} \left[\frac{1}{r} U_3^1(ra_n) - \frac{R(r^2-1)}{r^2(R^2-1)} U_3^1(Ra_n) + \frac{2(R^2-r^2)}{\pi r^2(R^2-1)}\right]$$

$$- \frac{1}{\sigma_{0,3}}\left[\frac{R^2(P_1 - P_R)}{(R^2-1)r^2} - \frac{P_1 - R^2P_R}{R^2-1}\right] \qquad (31b)$$

Axial Stress

Case (a): $\epsilon_z = 0$

$$\left(\frac{\xi S_z}{a_z B - \xi S_{zr}}\right) \frac{\sigma_z}{\sigma_{0,3}} = \frac{\beta\left(\frac{T_R}{T_g} - 1\right)}{1+\beta \ell nR}\left(\frac{R^2 \ell nR}{R^2-1} - \ell nr - \tfrac{1}{2}\right) + \sum_{n=1}^{\infty} \frac{F_3(a_n)e^{-a_n^2\tau}}{a_n^2} \left[\frac{2R}{R^2-1} U_3^1(Ra_n) + a_n^2 U_3(ra_n) + \frac{4}{\pi(R^2-1)}\right]$$

$$- \left(\frac{a_z B}{a_z B - \xi S_{zr}}\right) \left\{\frac{T_R}{T_g} + \beta \ell nR + \frac{\left(\frac{T_R}{T_g} - 1\right)(2R^2 \ell nR - R^2 + 1)\beta}{2(R^2-1)(1+\beta \ell nR)} + \sum_{n=1}^{\infty} \frac{F_3(a_n)e^{-a_n^2\tau}}{a_n^2} \left[\frac{2R U_3^1(Ra_n)}{R^2-1} + \frac{4}{\pi(R^2-1)}\right]\right\}$$

$$- \frac{2S_{zr}}{S_z \sigma_{0,3}} \left(\frac{\xi S_z}{a_z B - \xi S_{zr}}\right)\left(\frac{P_1 - R^2P_R}{R^2-1}\right) \qquad (31c)$$

Case (b): $F_z = 0$

$$\left(\frac{\xi S_z}{a_z B - \xi S_{zr}}\right) \frac{\sigma_z}{\sigma_{0,3}} = \frac{\beta\left(\frac{T_R}{T_g} - 1\right)}{1+\beta \ell nR}\left(\frac{R^2 \ell nR}{R^2-1} - \ell nr - \tfrac{1}{2}\right) + \sum_{n=1}^{\infty} \frac{F_3(a_n)e^{-a_n^2\tau}}{a_n^2} \left[\frac{2R}{R^2-1} U_3^1(Ra_n) + a_n^2 U_3(ra_n) + \frac{4}{\pi(R^2-1)}\right] \qquad (31d)$$

Characteristic Stress

$$\sigma_{0,3} = \frac{\xi T_g}{B} = \frac{E_r E_z (a_z \mu_{zr} + a_r) T_g}{E_z - \mu_{zr}^2 E_r} \qquad (31e)$$

3.5 Maximum Tensile and Compressive Stresses

The stress distributions in a hollow cylinder with a wall ratio of 2.0 were calculated in the absence of internal and external pressures. The maximum tensile and compressive stresses for various values of Biot's modulus and wall ratio were also determined. Based on these maximum stresses, the maximum gas temperatures which can be applied to the inside of the hollow cylinders have been calculated. The room-temperature physical properties used in the calculation are listed in Table 5.

Table 5. Properties of Graphite Materials Used in Numerical Calculations

	Grade ATJ	Grade ZTA
E_r, lb/in^2	1.40×10^6	2.40×10^6
E_z, lb/in^2	1.15×10^6	0.90×10^6
μ_{zr}, $\mu_{r\theta}$	0.20 (assumed)	0.20 (assumed)
α_r, 10^{-6}/°C	2.34	0.80
α_z, 10^{-6}/°C	3.46	7.20
$\bar{\sigma}_z$ (tension), lb/in^2	2,953	1,505
$\bar{\sigma}_z$ (compression), lb/in^2	8,530	12,400
$\bar{\sigma}_\theta$ (tension), lb/in^2	3,163	4,375
$\bar{\sigma}_\theta$ (compression), lb/in^2	8,330	7,100
B, 10^{-6} lb/in^2	0.679	0.372
ξ, 10^{-6} lb/in^2	3.032	2.24

In all cases, the temperature at the outside of the cylinder was assumed to be kept at zero. The increase of the temperature at the outside surface during the test firing has been found to be quite small.[13] Bradshaw[2] has pointed out that the assumption of zero temperature at the outside surface is a reasonable one for practical purposes.

The stress distributions in the hollow cylinders as a function of Fourier's modulus (dimensionless time) are plotted in Figures 4 to 10. These figures illustrate how the stresses build up during the transient period. Since Case I is a special case of Case III, these two cases are combined in most of the figures.

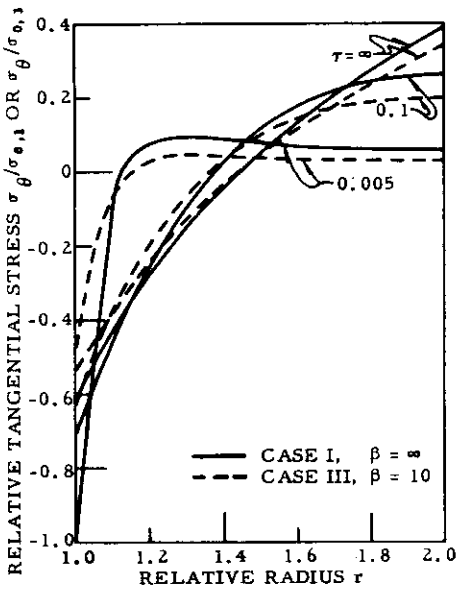

N-4295

Figure 4. Tangential Stress Distribution in Hollow Cylinder with Wall Ratio of 2.0. Cases I and III.

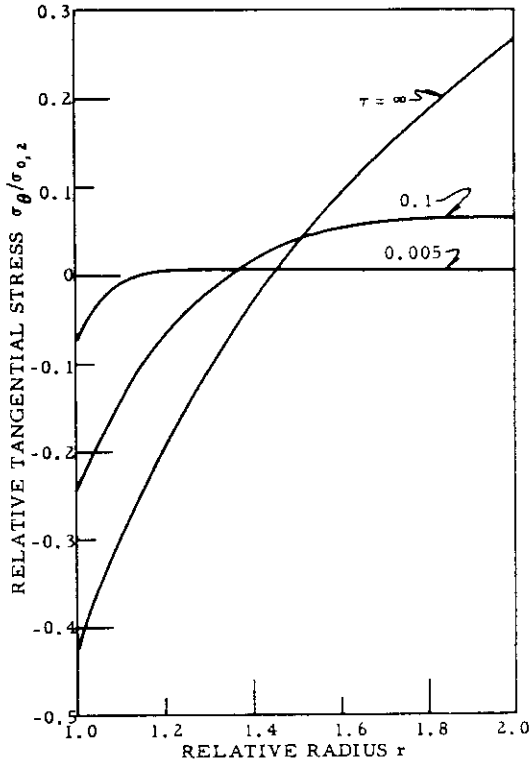

N-4296

Figure 5. Tangential Stress Distribution in Hollow Cylinder with Wall Ratio of 2.0. Case II.

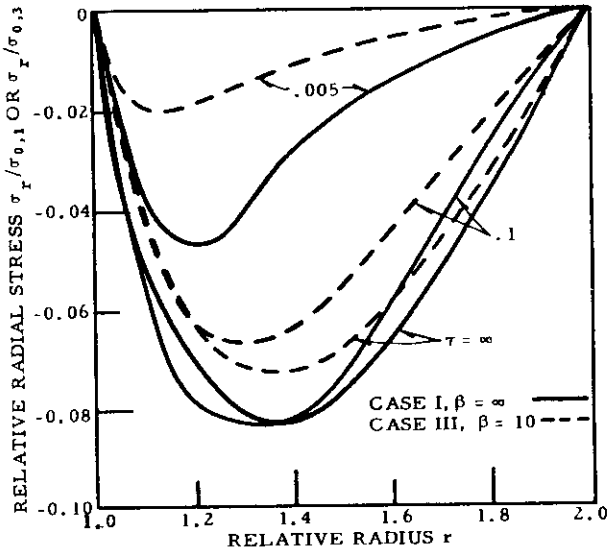

N-3539

Figure 6. Radial Stress Distribution in Hollow Cylinder with Wall Ratio of 2.0. Cases I and III.

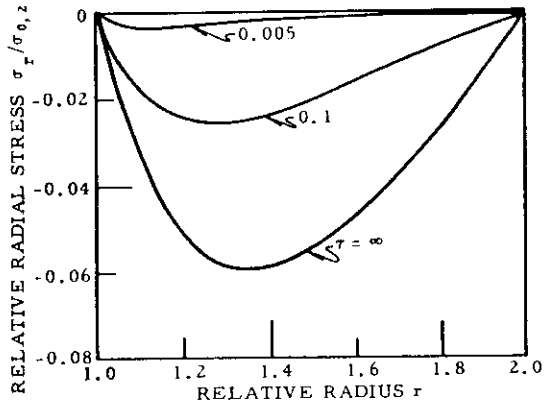

N-4297

Figure 7. Radial Stress Distribution in Hollow Cylinder with Wall Ratio of 2.0. Case II.

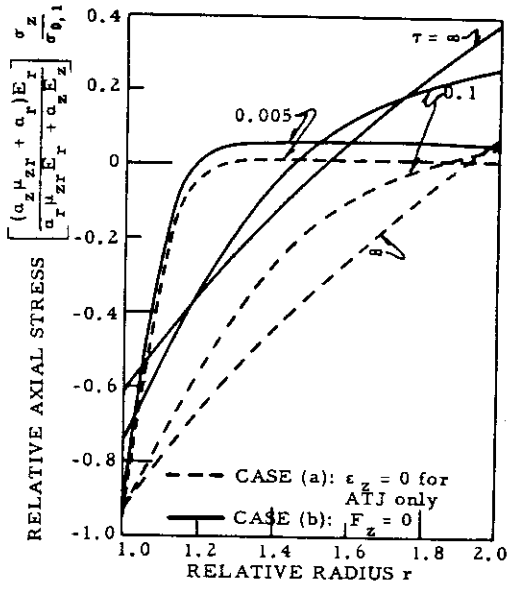

N-4305

Figure 8. Axial Stress Distribution in Hollow Cylinder with Wall Ratio of 2.0. Case I ($\beta = \infty$).

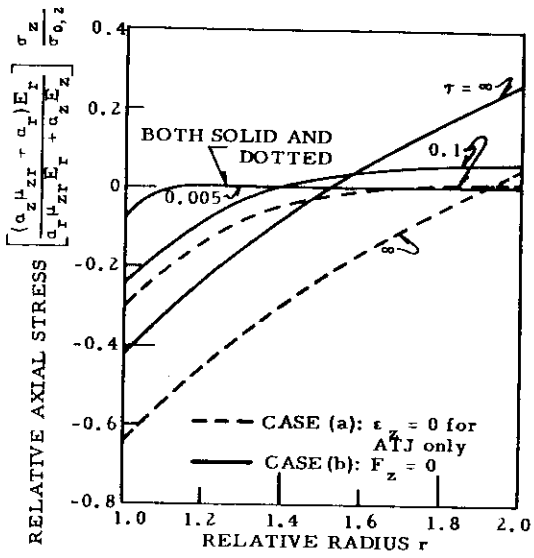

N-4298

Figure 9. Axial Stress Distribution in Hollow Cylinder with Wall Ratio of 2.0. Case II.

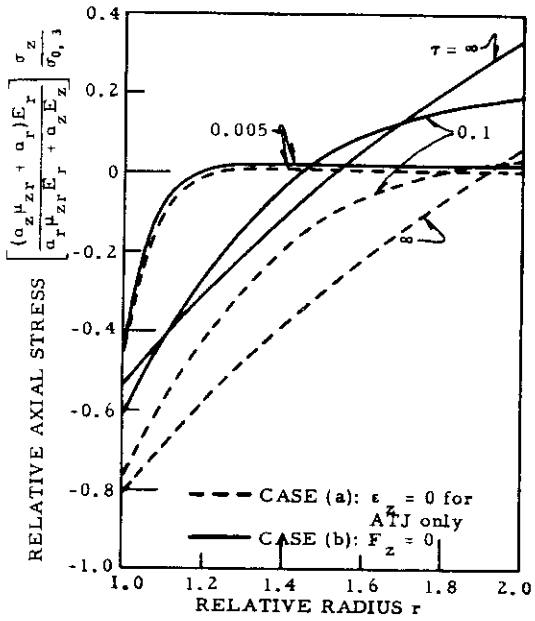

N-3216

Figure 10. Axial Stress Distribution in Hollow Cylinder with Wall Ratio of 2.0. Case III ($\beta = 10$).

The tangential stress distributions are shown in Figures 4 and 5, and the radial stress distributions are presented in Figures 6 and 7. The radial stresses are always compressive and are small in magnitude compared to the tangential stresses. The transient compressive tangential stress distribution for Case II is much less than those for Cases I and III at small times. In particular the compressive stress at the bore is initially infinite for Case I and is zero for Case II.

In Figures 8 to 10, the axial stress distributions are shown. The axial stresses for Case (a), zero axial elongation, and Case (b), zero normal force, are included. The axial stress for the case of zero axial elongation was calculated only for grade ATJ graphite, because the axial stress for this case depends on the physical properties of the material in such a way that the physical constants cannot be factored out in the stress equations. Therefore, the axial stress for this case must be calculated for each particular material.

The axial tensile stress is reduced considerably when the external forces are applied to the ends of the cylinder to prevent axial elongation. It has been observed that radial cracking is often the type of fracture exhibited by some of thegraphite nozzles which have been test fired. This type of fracture, perhaps, can be avoided if the ends of the nozzles are constrained properly.

The maximum tensile and compressive stresses for various values of Biot's modulus and wall ratio are investigated for Case (b), $F_z = 0$. The maximum tensile and compressive stresses always occur at the surfaces of the cylinder where the radial stress vanishes. Therefore, at the surfaces the axial stress is proportional to the tangential stress. It follows from equation (27) that at the surfaces

$$\sigma_\theta = \frac{E_r(\mu_{zr}\alpha_z + \alpha_r)}{\mu_{zr}\alpha_r E_r + \alpha_z E_z}\,\sigma_z \tag{32}$$

If we define the maximum relative tangential stress σ_θ^* at a surface by

$$\sigma_\theta^* = \frac{\sigma_\theta}{\sigma_{0,3}} \tag{33}$$

and the maximum relative axial stress σ_z^* at a surface by

$$\sigma_z^* = \frac{E_r(\mu_{zr}\alpha_z + \alpha_r)}{\mu_{zr}\alpha_r E_r + \alpha_z E_z}\,\frac{\sigma_z}{\sigma_{0,3}}\,, \tag{34}$$

then it follows from equations (32) to (34) that

$$\sigma_\theta^* = \sigma_z^* \quad ; \tag{35}$$

these formulas may be applied to Case III and also to Case I by letting $\beta = \infty$ and setting $T_g = T_1$. Hence the following remarks and Figures 11 and 13 may be applied to both the maximum relative axial and maximum relative tangential stresses.

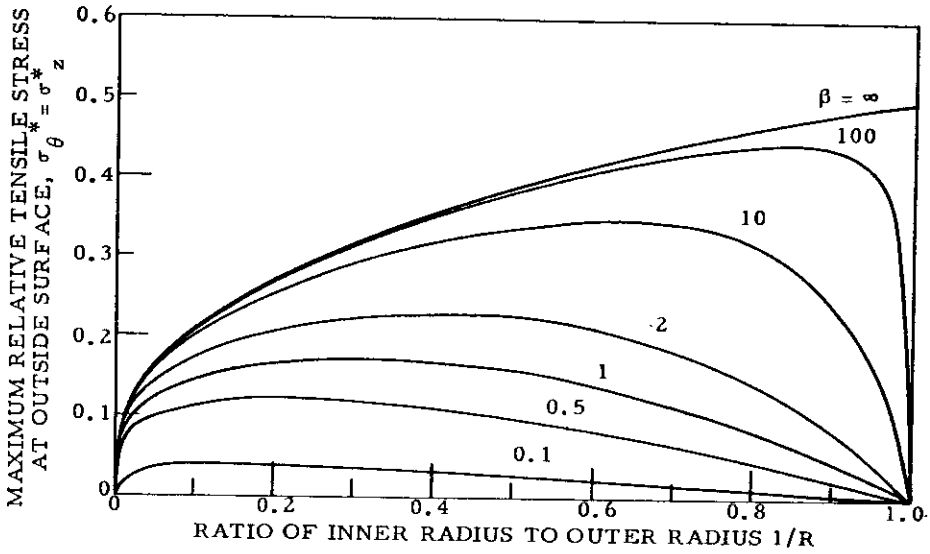

N-4299

Figure 11. Maximum Relative Tensile Stress at Outside Surface for Various Wall Ratios

The maximum tensile stresses within the cylinder always occur at the outside surface of the cylinder in the steady-state. These stresses are plotted for various values of Biot's modulus and wall ratio in Figure 11. On the other hand, the maximum compressive stresses do not always occur at the steady-state. The time at which the maximum compressive stress occurs is dependent on the wall ratio of the cylinder and Biot's modulus. Nevertheless, the maximum compressive stress always occurs at the bore of the cylinder. In Figures 12 and 13, the steady-state relative compressive stress, which is defined similarly to equation (34), and the maximum relative compressive stress are plotted, respectively, for various values of Biot's modulus and wall ratio. Comparing Figures 12 and 13, it can be seen that the steady-state compressive stress is also the maximum compressive stress for most cases. However, the magnitude of the maximum compressive stress is considerably greater than the steady-state compressive stress when Biot's modulus is large and the cylinder is thick. This can be seen clearly by comparing the curves for $\beta = 100$ in Figures 12 and 13. This illustrates the fact that the transient component cannot be neglected in the

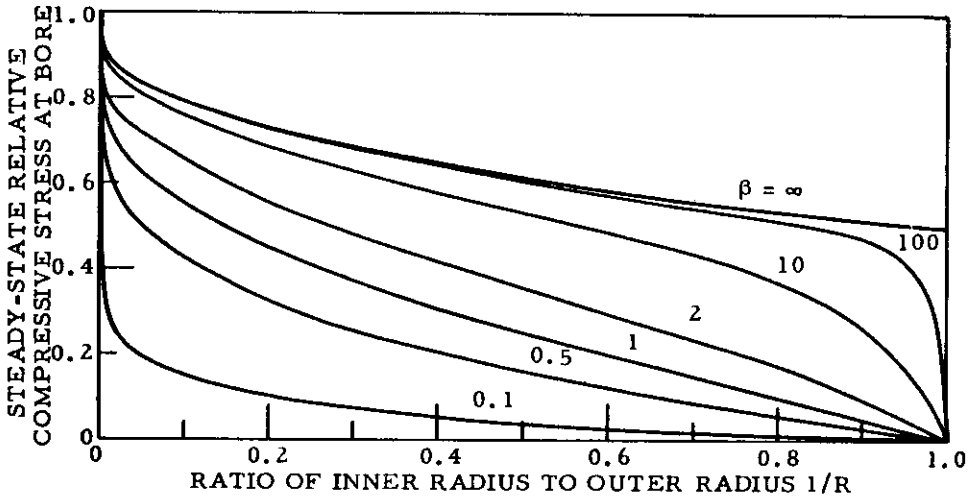

N-4300

Figure 12. Steady-State Relative Compressive Stress at Bore for Various Wall Ratios

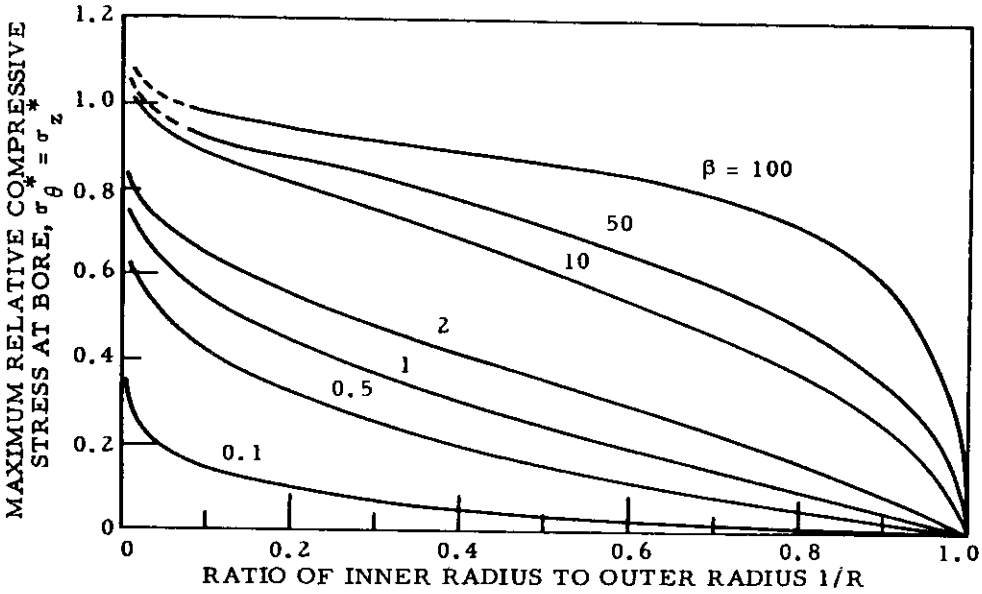

N-4311

Figure 13. Maximum Relative Compressive Stress at Bore for Various Wall Ratios

calculation of the maximum compressive stress in the case of a large Biot's modulus and a thick cylinder. In Figure 13, the curve for an infinite Biot's modulus (Case I) is not shown, because the maximum compressive stress theoretically becomes infinitely large at zero time and therefore is physically meaningless.

The normal stresses σ_θ, σ_r, and σ_z are also the principal stresses because there is no shearing stress on the planes on which σ_θ, σ_r, and σ_z act. The shearing stresses, which are developed on the planes making angles of 45 degrees with the θr, $z\theta$, and zr planes, are $\frac{1}{2}(\sigma_\theta - \sigma_r)$, $\frac{1}{2}(\sigma_r - \sigma_z)$, and $\frac{1}{2}(\sigma_z - \sigma_\theta)$. The magnitudes of the shearing stresses are large on both surfaces and very small in the central region between the surfaces. The maximum shearing stresses for both cases (a) and (b) occur at the bore and are equal to $\sigma_z/2$.

3.6 Maximum Gas Temperature and Criterion for Thermal Shock Resistance

The maximum gas temperature and the thermal shock resistance criterion for an anisotropic hollow cylinder subjected to Case I and Case III temperature boundary conditions and the end condition given by Case (b) will be examined in this section. Based on the maximum stress theory of failure, the maximum gas temperature which can be applied to the inside of the cylinder can be calculated from the maximum relative stresses and the fracture stresses of the materials in uniaxial tension and compression.

Maximum relative tensile tangential and axial stresses both occur at the outside surface of the cylinder at the steady-state condition. According to the maximum stress theory of failure, the cylinder will fracture if the tensile thermal stress at the outside surface becomes larger than the tensile fracture stress of the material. Therefore, if $\bar{\sigma}_\theta$ is the tensile fracture stress of the material in the tangential direction, the condition determining thermal failure is

$$\sigma_\theta^* = \bar{\sigma}_\theta / \sigma_{0,3}. \tag{36}$$

The maximum relative tangential stress, according to equation (31a), is given by

$$\sigma_\theta^* = \frac{\beta}{1 + \beta \ln R} \left[\frac{1}{2} - \frac{\ln R}{R^2 - 1} \right] \tag{37}$$

and is shown in Figure 11. The maximum permissible gas temperature, T_g, obtained by solving equations (31e) and (36), is

$$T_g = \frac{B}{\xi} \frac{\bar{\sigma}_\theta}{\sigma_\theta^*} = \left[\frac{E_z - \mu_{zr}^2 E_r}{E_r E_z (\alpha_z \mu_{zr} + \alpha_r)} \right] \frac{\bar{\sigma}_\theta}{\sigma_\theta^*} . \tag{38}$$

Similarly, if $\bar{\sigma}_z$ is the tensile fracture stress in the axial direction, then the condition determining thermal failure under axial tension is

$$\sigma_z^* = \frac{E_r(\mu_{zr}\alpha_z + \alpha_r)}{\mu_{zr}\alpha_r E_r + \alpha_z E_z} \frac{\bar{\sigma}_z}{\sigma_{0,3}} \tag{39}$$

Since $\sigma_z^* = \sigma_\theta^*$, σ_z^* is given by equation (37) and is shown in Figure 11. The maximum permissible gas temperature, according to equations (31e) and (39), is

$$T_g = \frac{E_r(\mu_{zr}\alpha_z + \alpha_r)}{\mu_{zr}\alpha_r E_r + \alpha_z E_z} \frac{B}{\xi} \frac{\bar{\sigma}_z}{\sigma_z^*} = \frac{E_z - \mu^2_{zr} E_r}{E_z(\mu_{zr}\alpha_r E_r + \alpha_z E_z)} \frac{\bar{\sigma}_z}{\sigma_z^*} . \tag{40}$$

Since the properties of graphites in tension and compression are different, the material constants to be used in equations (38) and (40) for tensile failure should be determined by tension tests.

For the materials considered in this report, T_g calculated by equation (40) is smaller than that calculated by equation (38), because the following relationship applies to these materials:

$$\frac{\bar{\sigma}_\theta}{E_r(\alpha_z\mu_{zr} + \alpha_r)} > \frac{\bar{\sigma}_z}{(\mu_{zr}\alpha_r E_r + \alpha_z E_z)}$$

For this reason equation (40) should be used for the calculation of the maximum gas temperature which will produce tensile thermal failure.

Thermal failure may also occur by compressive stress at the inside surface. Equations (36), (38), (39), and (40) may also be applied to thermal failure under compression provided that $\sigma_\theta^* = \sigma_z^*$ is interpreted as the maximum relative compressive stress shown in Figure 13, and the material properties to be used should be determined by uniaxial compressive tests. Since Young's moduli in compression for grade ATJ and grade ZTA graphites are not available, Young's moduli in tension of these materials will be used in the numerical calculations. For grade ATJ graphite, T_g calculated by equation (40) is smaller than that calculated by equation (38), because the inequality relationship given above still holds for grade ATJ graphite under this condition. Conversely, for grade ZTA graphite, T_g calculated by equation (38) is smaller than that calculated by equation (40), because under this condition the following relationship applies to grade ZTA graphite.

$$\frac{\bar{\sigma}_\theta}{E_r(\alpha_z\mu_{zr} + \alpha_r)} < \frac{\bar{\sigma}_z}{(\mu_{zr}\alpha_r E_r + \alpha_z E_z)}$$

Therefore, for the calculation of the maximum gas temperature which will produce compressive thermal failure equation (40) should be used for grade ATJ graphite and equation (38) should be used for grade ZTA graphite. The T_g calculated by the compressive fracture stress and material constants in compression must be compared with T_g calculated by the tensile fracture stress and material constants in tension. The smaller T_g is considered as the critical gas temperature for a hollow cylinder.

Maximum gas temperatures for grade ATJ and grade ZTA graphites are plotted, respectively, in Figures 14 and 15 for Cases I and III boundary

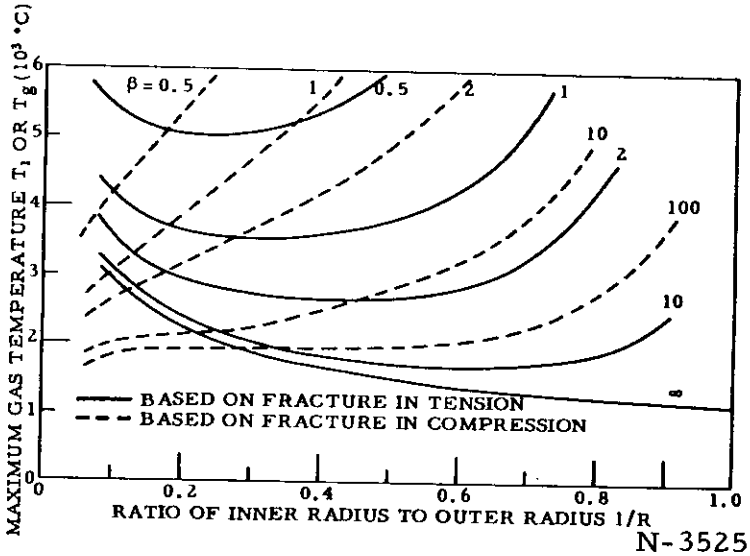

Figure 14. Maximum Gas Temperature Predicted for Grade ATJ Graphite, for Cases I and III.

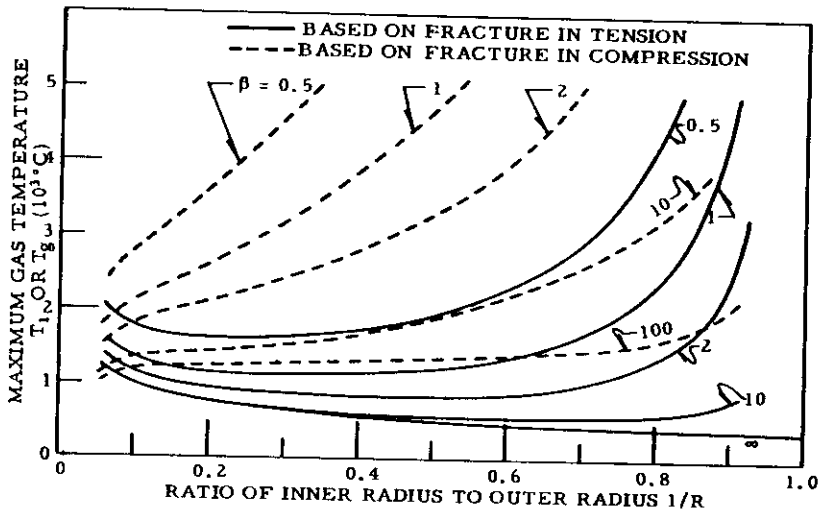

Figure 15. Maximum Gas Temperature Predicted for Grade ZTA Graphite, for Cases I and III.

conditions. A grade ZTA graphite cylinder exhibits lower thermal shock resistance than a grade ATJ graphite cylinder. This is partly due to the high degree of anisotropy and low tensile strength in the against-grain direction of grade ZTA graphite. From these figures it can be noted that the axial tensile stress at the outside is generally the critical stress in thin to moderately thick hollow cylinders. The maximum compressive stress can become the critical stress for extremely thick hollow cylinders and large values of Biot's modulus.

Equation (40) also gives the criterion for the evaluation of thermal shock resistance of the material. A material which gives a high value of T_g is considered to have a high thermal shock resistance. Equations (38) and (40) reduce to the following equation in the isotropic case,

$$T_g = \frac{1 - \mu}{\alpha E} \frac{\bar{\sigma}}{\sigma^*} \quad . \tag{41}$$

Buessem[14] found for a solid cylinder that the reciprocal of σ^* can be approximated by $2.0 + 4.3/\beta$ for a limited range of β. He suggested that the maximum gas temperature which can be applied to the outside surface of a solid cylinder of radius, a, is determined by

$$T_g = 2.0\, R' + \frac{4.3\, R''}{ah} \quad , \tag{42}$$

where $R' = \frac{(1 - \mu)\bar{\sigma}}{\alpha E}$, first thermal stress resistance factor,

and $R'' = \frac{(1 - \mu)k\bar{\sigma}}{\alpha E}$, second thermal resistance factor.

It follows that when the heat transfer coefficient h is large T_g is independent of the thermal conductivity k, and conversely, when h is small T_g is approximately proportional to k. From equation (37) one observes that $\sigma_\theta^* = \sigma_z^*$ is independent of $\beta = ah/k_r$ when β is large (for example, Case I) and is approximately proportional to β when β is small. Therefore, the results given above form a generalization of known results for isotropic materials to anisotropic materials.

The effect of anisotropy on T_g can be best illustrated by numerical examples. For this purpose the values of $T_g \sigma^*$ were calculated by equations (38), (40), and (41) and are given in Table 6. The material constants given in Table 5 are used in the calculations. Two values of $T_g \sigma^*$ are calculated by equation (41): one calculated with the material constants in the with-grain direction, and the other calculated with the material constants in the against-grain direction.

The per cent deviation in Table 6 represents the error which results from the assumption of isotropy. A negative sign indicates that the isotropic

Table 6. Values of $T_{g^{\sigma}}$*

	Material	Anisotropic Case		Isotropic Case			
		$T_{g^{\sigma}\theta}$* Eq. (38) (°C)	$T_{g^{\sigma}z}$* Eq. (40) (°C)	$T_{g^{\sigma}\theta}$* Eq. (41) WG Properties (°C)	% Dev. from Eq. (40) (%)	$T_{g^{\sigma}z}$* Eq. (41) AG Properties (°C)	% Dev. from Eq. (40) (%)
Tension	Grade ATJ	709	606	772	+27.4	594	-2.0
Tension	Grade ZTA	727	196	1823	+830.1	186	-5.1
Compression	Grade ATJ	1865	1750	2033	+16.2	1715	-2.0
Compression	Grade ZTA	1179	1614	2958	+83.3	1531	-5.1

calculation based on the properties in the against-grain direction underestimates the thermal shock resistance of the material. A positive sign indicates that the isotropic calculation based on the properties in the with-grain direction overestimates the thermal shock resistance of the material. A thermal stress analysis based on isotropic theory and the properties in the against-grain direction may give sufficiently accurate results for engineering purposes. The thermal shock resistance estimated in this way is only 5.1 per cent less than the anisotropic calculation for grade ZTA graphite. The thermal shock resistance computed with the properties in the with-grain direction is nearly 9.0 times larger than that computed by the anisotropic formula for grade ZTA graphite.

It should be noted that the conclusions derived from this investigation are valid only for a hollow cylinder under the condition of plane strain. Perhaps the strength and grain orientation of the materials such as grades ATJ and ZTA graphites can be best utilized under the condition of plane stress, for under this condition the axial stress becomes very small.

4. SUDDEN COOLING OF HEATED HOLLOW CYLINDERS

It has been established that for most cases the axial stress at the outside surface is the maximum tensile stress during the firing. Therefore, if fracture occurs during the firing, it would initiate at the outside surface and propagate radially inward.

Frequently the nozzle is quenched by spraying water into the bore immediately after the completion of the test firing in order to permit early visual inspection. It is possible that fracture could result from the rapid cooling.

In this section, the stress distributions in hollow cylinders during rapid cooling are investigated. The test firing time of nozzles is approximately 50 seconds and by the end of the test firing the steady-state temperature distribution is nearly reached within the nozzle. Therefore, it is sufficiently accurate to assume that the bore temperature of a hollow cylinder, which initially has a known temperature distribution, is suddenly brought down to zero and maintained at that temperature. The initial temperature distribution within the cylinder is assumed to be identical to the steady-state temperature distribution of Case I. The boundary conditions for the cooling process can be written as:

$$\left.\begin{aligned} T &= T_1 \frac{\ln \frac{R}{r}}{\ln R} \quad \text{when } t = 0 \\ T &= 0 \text{ at } r = 1 \text{ and } R \text{ when } t > 0. \end{aligned}\right\} \tag{43}$$

The temperature and stress distributions during the cooling process, in the absence of the external and internal pressures, can be obtained in a similar manner to that in the previous section. These are

Temperature

$$T = \sum_{n=1}^{\infty} F_1(\alpha_n) e^{-\alpha_n^2 \tau} U_1(r\alpha_n) \tag{44a}$$

Tangential Stress

$$\frac{\sigma_\theta}{\sigma_{0,1}} = -\sum_{n=1}^{\infty} \frac{F_1(\alpha_n) e^{-\alpha_n^2 \tau}}{\alpha_n^2} \left[\frac{R(r^2+1)}{r^2(R^2-1)} U_1'(R\alpha_n) + \frac{U_1'(r\alpha_n)}{r} + \alpha_n^2 U_1(r\alpha_n) + \frac{2(R^2+r^2)}{\pi(R^2-1)r^2} \right] \tag{44b}$$

Radial Stress

$$\frac{\sigma_r}{\sigma_{0,1}} = \sum_{n=1}^{\infty} \frac{F_1(a_n)e^{-a_n^2\tau}}{a_n^2} \left[\frac{U_1'(ra_n)}{r} - \frac{R(r^2-1)}{r^2(R^2-1)} U_1'(Ra_n) + \frac{2(R^2-r^2)}{\pi(R^2-1)r^2} \right] \quad (44c)$$

Axial Stress

For Case (a): $\varepsilon_z = 0$

$$\left(\frac{\xi s_z}{a_z B - \xi s_{zr}}\right) \frac{\sigma_z}{\sigma_{0,1}} = - \sum_{n=1}^{\infty} \frac{F_1(a_n)e^{-a_n^2\tau}}{a_n^2} \left[\frac{2R}{R^2-1} U_1'(Ra_n) + a_n^2 U_1(ra_n) + \frac{4}{\pi(R^2-1)} \right]$$

$$+ \left(\frac{a_z B}{a_z B - \xi s_{zr}}\right) \sum_{n=1}^{\infty} \frac{F_1(a_n)e^{-a_n^2\tau}}{a_n^2} \left[\frac{2R}{R^2-1} U_1'(Ra_n) + \frac{4}{\pi(R^2-1)} \right] \quad (44d)$$

For Case (b): $F_z = 0$

$$\left(\frac{\xi s_z}{a_z B - \xi s_{zr}}\right) \frac{\sigma_z}{\sigma_{0,1}} = - \sum_{n=1}^{\infty} \frac{F_1(a_n)e^{-a_n^2\tau}}{a_n^2} \left[\frac{2R}{R^2-1} U_1'(Ra_n) + a_n^2 U_1(ra_n) + \frac{4}{\pi(R^2-1)} \right] \quad (44e)$$

Comparing equations (29) and (44), one will note that equation (44) is identical to the negative of the transient components of equation (29). In Figures 16, 17, 18, and 19, the temperature and stress distributions during the cooling period are shown. In these figures, the initial distribution is indicated by the dotted line. During the rapid cooling the relative tangential and axial stresses at both surfaces of the cylinder become tensile stresses equal in magnitude. Under such a state of severe biaxial tension, it is possible that fracture might initiate at the bore during the cooling period if the bore surface is already damaged by ablation during the test firing. Therefore, in some cases the fracture of the rocket nozzle could be caused by rapid cooling after the test firing, even if fracture did not occur during the heating process.

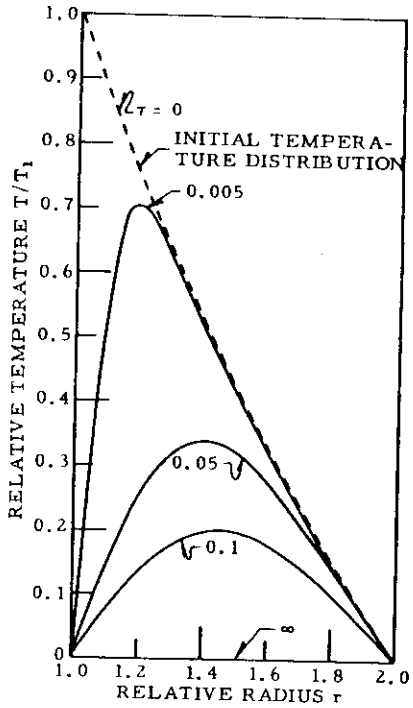

N-2797

Figure 16. Temperature Distribution in Hollow Cylinder with Wall Ratio of 2.0 During Cooling.

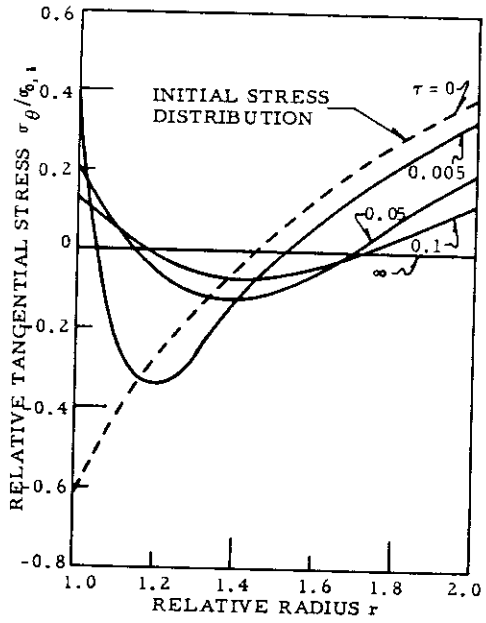

N-4301

Figure 17. Tangential Stress Distribution in Hollow Cylinder with Wall Ratio of 2.0 During Cooling.

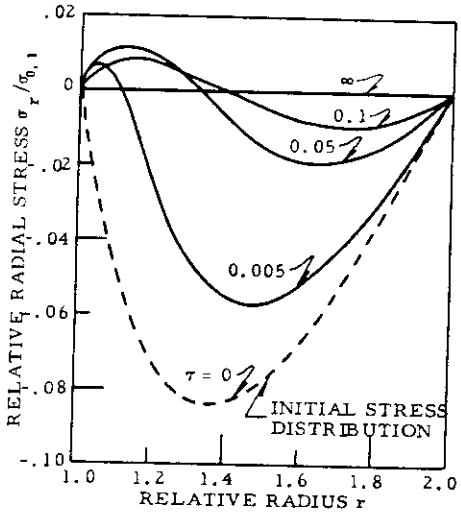

N-4302

Figure 18. Radial Stress Distribution in Hollow Cylinder with Wall Ratio of 2.0 During Cooling.

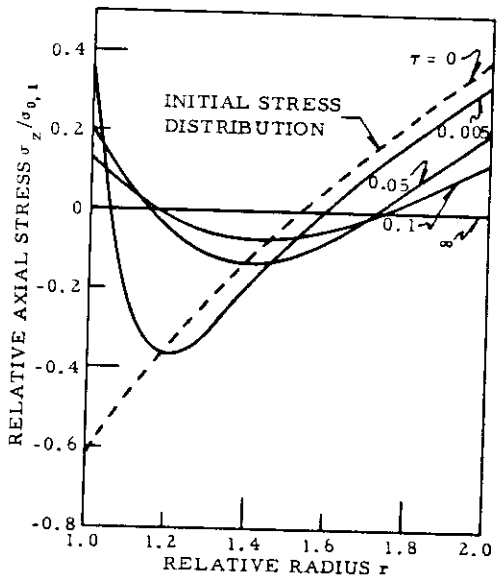

N-4304

Figure 19. Axial Stress Distribution in Hollow Cylinder with Wall Ratio of 2.0 During Cooling.

5. SUMMARY AND CONCLUSIONS

Thermal stresses generated in anisotropic hollow cylinders have been investigated by the quasi-static thermal elasticity theory. Numerical examples were treated for grades ATJ and ZTA graphites.

The hollow cylinders were assumed to be transversely isotropic. The physical and thermal properties in the with-grain direction are different from those in the against-grain direction. The properties of the materials were assumed to be independent of temperature. The axis of symmetry of the hollow cylinder coincides with the against-grain direction of the material.

Three thermal boundary conditions were assumed in this analysis. The following thermal conditions were imposed on the bore of the hollow cylinder which was initially at zero or room temperature: (1) the bore temperature is suddenly increased to a finite value; (2) a constant heat flux is suddenly applied at the bore; and (3) heat flow occurs at the bore by convection. In all these cases the temperature of the outside surface is maintained at zero or initial temperature.

Based on these temperature distributions, the transient and steady-state thermal stresses in the hollow cylinder were calculated for a cylinder with a wall ratio of 2.0. Maximum tensile and compressive stresses generated were calculated for various values of Biot's modulus ($\beta = ah/k_r$) and wall ratio. The steady-state axial tensile stress at the outside surface is also the maximum tensile stress. Maximum compressive stress always occurs at the bore. If Biot's modulus is small, the maximum compressive stress occurs at the steady-state condition. If Biot's modulus is large, the maximum compressive stress occurs during the transient period. Therefore, in this case, the transient solution cannot be neglected in stress analysis. Since the tensile strength in the axial direction of the graphite cylinder is relatively low, thermal failure generally occurs under the axial tensile stress at the outside surface. If the values of Biot's modulus and wall ratio are extremely large, thermal failure due to the compressive stress at the bore may occur.

The maximum temperature which can be applied to the bore of the cylinder was calculated from the values of the maximum thermal tensile and compressive stresses and from the fracture stresses measured in tensile and compression tests. It was found that grade ATJ graphite cylinders have a higher thermal shock resistance than grade ZTA graphite cylinders.

Effects of anisotropy on thermal shock resistance of graphites have been examined. Thermal shock resistance calculated by the isotropic formula and the properties in the with-grain direction is found to be too high. Calculations based on the isotropic formula and the properties in the against-grain direction underestimate slightly thermal shock resistance of graphite; however, it is sufficiently accurate for many practical engineering problems.

A problem of the sudden cooling of a hollow cylinder with a known initial temperature distribution has been investigated in connection with the problem of the sudden cooling of the rocket nozzles after test firing for visual inspection. It is found that a high tensile stress is built up at the bore during cooling. The magnitude of the tensile stress is equal to the tensile stress at the outside surface but is not greater than the initial tensile stress which existed at the outside surface. It is possible that fracture might initiate at the bore due to rapid cooling if the bore surface were already damaged by ablation during the test firing.

The material presented in this report constitutes the first phase of the analysis of thermal stresses in an anisotropic hollow cylinder. In this analysis, the material properties have been assumed to be independent of temperature. In the second phase of the analysis, the material properties will be treated as temperature dependent variables. A preliminary study has been made on thermal stresses in an ATJ graphite hollow cylinder by the isotropic theory developed by Stanišić and McKinley.[7] In the isotropic case and under steady-state conditions, the calculated thermal stresses in the cylinder increased significantly when the variations of the material properties with temperature were considered. The effect of the increase in stress is partially compensated by the increase of the strength of graphite with temperature. These calculations must be generalized by including elastic anisotropy and transient solutions.

6. REFERENCES

1. J. C. Jaeger, "On Thermal Stresses in Circular Cylinders," Phil. Mag. 36, 1945, pp. 418-428.

2. F. J. Bradshaw, "Thermal Stresses in Non-Ductile High Temperature Materials," Technical Note No. Met 100, British Aircraft Establishment, Feb. 1949.

3. H. H. Hilton, "Thermal Stresses in Bodies Exhibiting Temperature-Dependent Elastic Properties," J. Appl. Mech. (ASME), 19, No. 3, 1952, pp. 350-4.

4. Chieh-Chien Chang and Wen-Hwa Chu, "Stresses in a Metal Tube Under Both High Radial Temperature Variation and Internal Pressure," J. Appl. Mech. 21, 1954, pp. 101-8.

5. R. Trostel, "Wärmespannungen in Hohlzylindern mit Temperaturabhängigen Stoffwerten," Ingenieur Archiv 26, 1958, pp. 134-42.

6. R. Trostel, "Stationäre Wärmespannungen mit Temperatur abhängigen Stoffwerten," Ingenieur Archiv 26, 1958, pp. 416-34.

7. M. M. Stanišić and R. M. McKinley, "A Note on Thermal Stresses in Hollow Cylinders," Ingenieur Archiv 27, 1959, pp. 227-41.

8. J. J. Thompson, "A Note on Thermo-elastic Stress in Axially Symmetric Anisotropic Cylinders," AAEC/E32, August, 1958.

9. J. D. Batchelor, S. W. McCormick, R. K. White, E. L. Olcott, and E. F. Ford, "Improvement of the Usefulness of Pyrolytic Graphite in Rocket Motor Applications," Atlantic Research Corp., Alexandria, Va., Quarterly Progress Report, June through August, 1961, Contract No. DA-36-034-ORD-3279 RD, Project No. TB 4-004, September 15, 1961.

10. H. S. Carslaw and J. C. Jaeger, "Conduction of Heat in Solids," Oxford University Press, 2nd Edition, 1959, p. 42.

11. A. E. H. Love, "A Treatise on the Mathematical Theory of Elasticity," Dover Publication, 4th Edition, Chapter III.

12. Bruno A. Boley and Jerome H. Weiner, "Theory of Thermal Stresses," John Wiley & Sons, Inc., March, 1960, pp. 246-49.

13. E. M. Sadownick, Aeronautical Systems Division, Wright-Patterson Air Force Base, Ohio, Report No. WADC-TR-59-602, Pt. II, "Investigation of Materials Capabilities of Material Systems in Solid Rocket Motors," Interim Report, February, 1962, 94p.

14. W. R. Buessem, "Thermal Shock," "High Temperature Technology," edited by I. E. Campbell, Chapman & Hall, 1956, pp. 460-83.